Journal of Seismology **2:** 47–64, 1998.

Ocean-generated microseismic noise located with the Gräfenberg array

A. Friedrich[1], F. Krüger[2] & K. Klinge[1,3]
[1] *Seismologisches Zentralobservatorium Gräfenberg, Erlangen, Germany*
[2] *Institut für Geowissenschaften, Universität Potsdam, Potsdam, Germany*
[3] *Bundesanstalt für Geowissenschaften und Rohstoffe (BGR), Hannover, Germany*

Received 1 July 1997; accepted in revised form 2 February 1998

Abstract

The main cause for mid-period seismic ground distortions are ocean waves generated by atmospheric disturbances. These act upon the earth through different mechanisms. The microseismic wavefield can be divided into primary ($T = 12$–18 s) and secondary ($T = 6$–9 s) noise. Classical theory tells that the origin of these induced ground distortions depends on the location and the intensity of the low pressure region.

A considerable part of the microseismic wave field reaches the GRF-array in southern Germany with high coherency and almost constant amplitudes. Thus it is possible to locate the generating areas using frequency-wavenumber analysis.

Five discrete generating areas for secondary microseisms and three generating areas for primary microseisms could be determined in the Atlantic Ocean, the Arctic Sea and the Mediterranean Sea by investigating broadband continuous recordings over four months in winter 1995/96. An essential result is the long-time constancy of the backazimuths of the coherent part of the microseismic wavefield with respect to the origin areas, independent of the location of the moving low pressure zone. Results from a triangulation using additionally broadband data from the NORSAR-array and an independent estimation of the distance of the source region with water wave dispersion data indicate an origin of the secondary microseismic wavefield near the north-Norwegian coast for the strongest source.

The array analysis of a temporary network of ten three-component broadband stations in south-east Germany shows that the ratio of energy between coherent Love and Rayleigh waves is much higher for the primary than for the secondary microseismic noise wavefield. This indicates differences in the source mechanisms.

Introduction

Ocean-generated microseisms are a constant source of energy in the mid-period band of seismic signals. A typical displacement power spectrum in Figure 1 shows that the ambient seismic noise is dominated by the two peaks of the primary microseisms at a period of about $T = 14$ s and the secondary microseisms at a period of about $T = 7$ s. The nature of these seismic sources is still not completely understood (Holcomb, 1989).

The investigation of ocean-generated microseisms dates back to the beginnings of seismology (for a summary see Gutenberg, 1924), when Wiechert (1904) proposed the relation between ocean swell on coasts and microseisms. Fundamental new progress was made, when Longuet-Higgins (1950) established a theory that explains the generation of secondary microseisms: Ocean waves of equal period travelling in opposite directions generate standing waves of half the period, which in their turn cause a non-linear pressure perturbation propagating without attenuation to the ocean bottom. Detailed observations about microseisms on land were done by Darbyshire (1950) and Iyer (1958). Hasselmann (1963) used a statistical approach to show that the random pressure fluctuations caused by the ocean waves are sufficient to generate microseisms of considerable amplitude. For primary microseisms, Haubrich et al. (1963) could demonstrate a close relationship between microseisms and swell at the beaches by comparison of the spectra of both data sets.

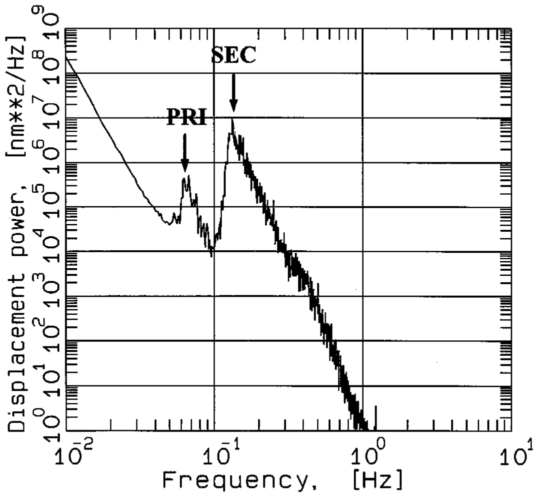

Figure 1. Typical displacement power spectrum showing the peaks corresponding to primary (PRI) and secondary (SEC) microseisms.

Starting with Gutenberg, several authors found areas of preferred generation of ocean induced microseisms. Strobach (1962) studied a source of secondary microseisms in northern Scandinavia. Using data of three 3-component stations Schmalfeldt (1978) could show that primary microseisms were generated at the north-German coast while a secondary microseismic source was acting near the Norwegian coast. Båth and Kulhánek (1990) recorded primary microseisms at a north-Swedish station (Umeå), coming from the entire north-Norwegian coast. Later Darbyshire (1991) discriminated two secondary microseismic sources located in the North Channel and the Bristol Channel.

Numerous investigations using array data have contributed to the understanding of the generation of primary and secondary microseisms. Lacoss et al. (1969) who investigated frequency-wavenumber spectra of microseisms recordings at LASA (Montana) demonstrated that the microseismic wavefield is dominated by fundamental mode Rayleigh waves at periods longer than 7 s, but that there also exist fundamental mode Love waves. Later Capon (1972) obtained similar results for the LASA, ALPA and NORSAR arrays. The microseismic noise situation at the NORSAR-array (Norway) was studied in detail by Bungum et al. (1971, 1985). Cessaro & Chan (1989) detected two simultaneously acting primary microseismic sources near the coasts of the North Atlantic and Pacific ocean using a wide-angle triangulation approach.

Primary microseisms are generated directly through gravity waves of the ocean. At a fixed point on the ocean bottom the height of the above water column changes permanently with the wave motion. The induced pressure perturbation then generates seismic waves of the same period (see Figure 12a). Primary microseisms are only induced directly at shores (for details see Section 4.1; Haubrich et al., 1963; Hasselmann, 1963).

The generation of secondary microseisms requires ocean waves travelling in opposite directions with equal periods (i.e. $\vec{k}_1 = -\vec{k}_2$, where $\vec{k}_1$ and $\vec{k}_2$ are the wave number vectors). According to Longuet-Higgins (1950) such constellations might occur in the centre of a cyclone due to oppositely travelling ocean waves arriving from all directions or through reflection on straight coastlines. The superposition of opposed waves leads to a standing wave with half a period. The evaluation of the Bernoulli-equation yields, that the variation of the mean pressure on the ocean bottom only depends on the product of the wave amplitudes (see Section 4.3). Hence the fluctuation of the mean pressure is independent of the ocean depth, i.e. pressure variations are able to propagate to infinite depth and induce microseisms of half the period of the ocean waves on ocean bottoms of arbitrary depth.

Contrary to short- and long-period bandlimited data, digital broadband data allow the investigation of the mid-period microseismic wavefield with high precision due to the linearity and high dynamics of modern feedback seismometers in the period range of microseisms. The broadband characteristic makes such data very suitable for a broadband frequency-wavenumber ($f - k$) analysis, which is a powerful tool for determining the backazimuth and the slowness of coherent seismic waves. It offers a much higher resolution in terms of backazimuth determination and source location than obtainable with classic methods (e.g. polarisation analysis of 3-component recordings) using a single 3-component station. Even more important is the possibility to discriminate several simultaneously active microseismic sources.

In this paper, we present the results of an array study with broadband data of the Gräfenberg-array (GRF) and a temporary broadband network (ANISO) in southern Germany (see Figure 2). Recordings of four months of continuous broadband GRF-array data were analyzed. For an outstanding 'event' of a very strong acting microseismic source (December, 16th and 17th of 1995), the microseismic wavefield was investigated in detail using additionally data of the temporary broadband network.

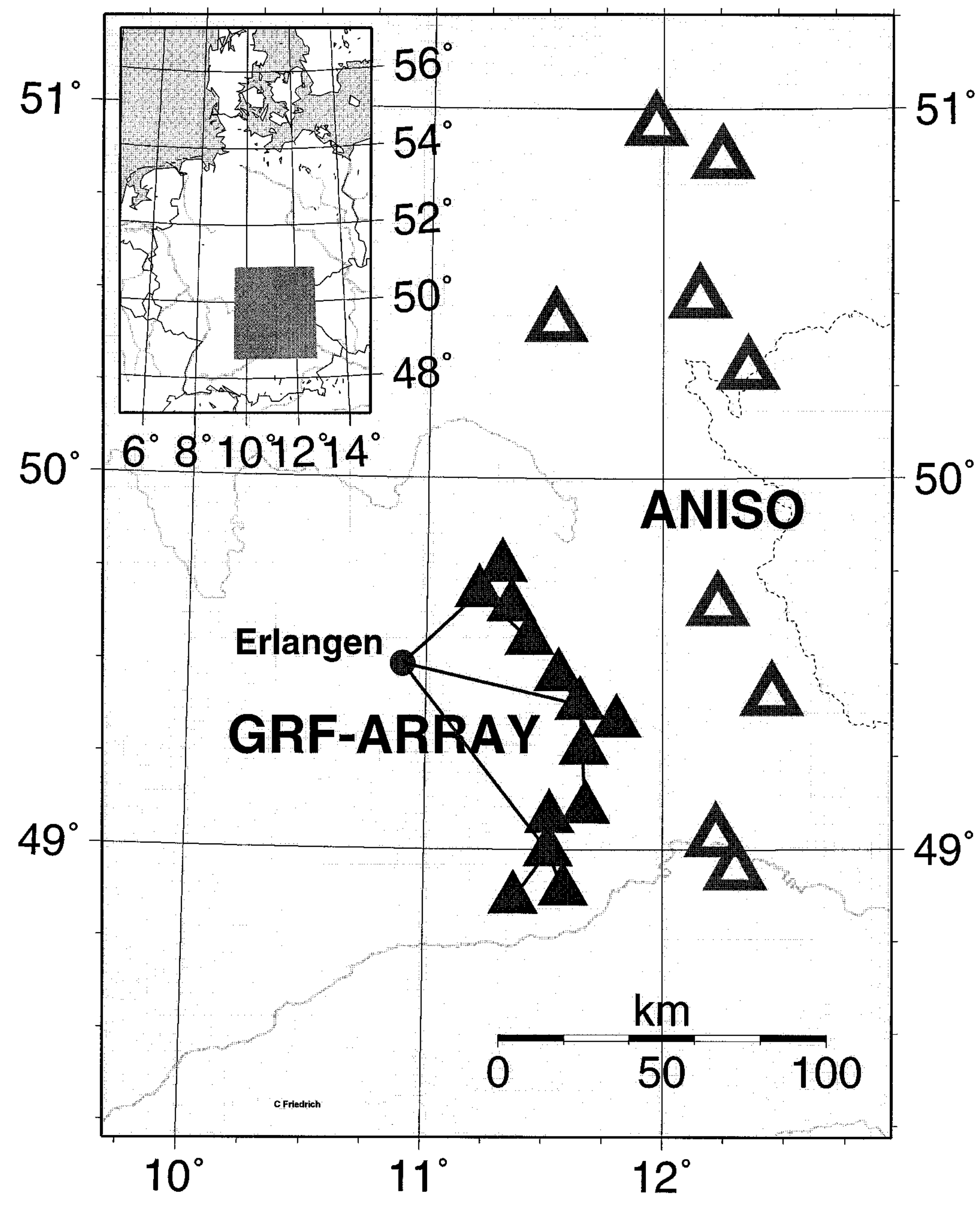

Figure 2. Location of the stations used, showing the Gräfenberg-array (GRF) and stations of the temporary network (ANISO).

Data and Processing

The GRF-array (Harjes & Seidl, 1978) is located in south-east Germany on jurassic limestone and consists of 13 vertical and three 3-component stations equipped with STS-1 seismometers, broadband from 5 Hz to 20 s (Wielandt & Streckeisen, 1982). The average intersta-tion distance and aperture makes the GRF-array very suitable for the analysis of microseisms. For the investigation of horizontally polarized seismic waves data of the above mentioned temporary network (ANISO), could be used, which was operated 150 km east of the GRF-array in the Vogtland area (10 out of 25 broad-

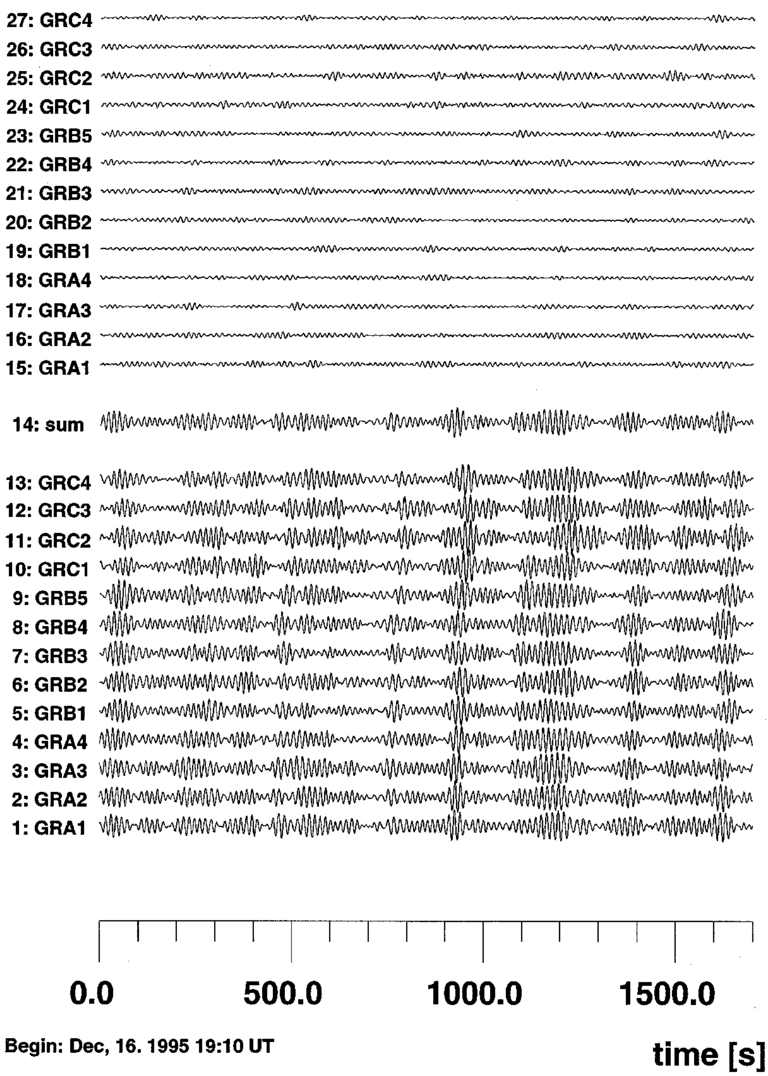

Figure 3. Bandpass filtered ($T = 12$–20 s) vertical component GRF-seismograms showing records of the primary microseisms (traces 1–13). Trace 14 shows the beam of all traces. The traces 15–27 are the difference traces between traces 1–13 and the beam (14) showing the incoherent part of the observed microseisms.

band triaxial STS-2 seismometers, see Wielandt & Steim, 1986).

The high coherency of bandpass-filtered GRF-array microseisms recordings (see Figure 3) initiated the idea to investigate the microseismic wavefield with a quasi-continuous frequency-wavenumber analysis in a moving time window. In the first processing step bandpass prefilters (from 12 s to 20 s for primary, and 6 s to 11 s for secondary microseisms) were applied to the GRF broadband data in order to improve the signal-to-noise ratio. In a second step frequency-wavenumber spectra were computed for a moving time window. We used a broadband frequency-wavenumber analysis algorithm (Kværna & Ringdahl, 1986) to extract optimally the slowness information present in the prefiltered broadband data. The length of the time window was set to 240 s in order to ensure that several wavelengths of the slowest expected wave (Rayleigh/Love wave over sediments) are recorded over the entire array. After storing the backazimuth, slowness and beampower results, the time window was shifted by 60 s to produce a continuous output stream. For a better overview, only time windows having their beam power maximum in the slowness range corresponding to surface waves (26–

44 s/°) were extracted and condensed in a plot of a complete month.

For computational reasons the slowness resolution was set to 1.1 s/° in the x- and y-direction. Hence, in the worst constellation of backazimuths of about 45°, the slowness values have an error of ±0.8 s/° due to the discrete sampling in the slowness space. The corresponding maximum error of backazimuth is therefore ±1.3° for the slowness range of interest.

Results

Backazimuth distribution of primary and secondary microseisms' source area

For recordings of October, November, December and January 1995/96, the results of the frequency-wavenumber analysis are presented for primary microseisms in Figure 4 and for secondary microseisms in Figure 5. Each diagram shows all days of a month on the x-axis and the backazimuths from –180° to 180° on the y-axis. A dot represents the detected energy maximum in a slowness and frequency window appropriate for primary and secondary microseisms for each time window, respectively.

Because only the beampower *maximum* is plotted for each time window, the backazimuth can change abruptly within a short time span in the case of simultaneously active sources and variable radiation power of each microseismic source. The inspection of the $f - k$ results for each time window shows that the distinct sources fade out and do not terminate abruptly. In case of strong earthquakes (e.g. December, 3rd 1995, 18:01:09, lat: 44.663 N lon: 149.300 E, depth: 33 km Mw = 7.9, Kuril Islands, backazimuth with respect to GRF is 30°) the wavefield can be dominated by coda waves for hours. In this case the lines of constant backazimuth are interrupted by widely scattered slowness and backazimuth values leading to gaps in the monthly plots due to the slowness windows applied. For real data gaps (i.e. missing data) the backazimuth was set to +180° in Figures 4 and 5.

With respect to primary microseisms, the backazimuths show a continuous distribution corresponding to west-European shorelines. Backazimuths from +10° to –25° (PRI 1 in Figure 4), –60° to –75° (PRI2) and –75° to –100° (PRI3) are more intense and mark preferred areas of strong primary microseisms generation (see also Table 1). For the time span 22nd to 23rd and 27th January additionally backazimuths between –110° and –150° show relatively strong microseisms. Furthermore, there are indications for a separate source region at –17° partially overlapped by PRI 1.

In contrast to the more continuous backazimuth distribution of the primary microseisms the secondary microseisms are clearly concentrated in five discrete backazimuths. The corresponding directions, marked in Figure 5, point towards the north Norwegian Sea (SEC1), the Atlantic Ocean (SEC2, SEC3, SEC4) and the Mediterranean Sea (SEC5). Figure 6 illustrates these five directions projected onto a map of Europe. Table 1 summarizes all areas of microseisms generation.

There are indications for additional source areas. Source SEC1 is probably composed of two or three nearby source areas at about +5°, +10° and +25° backazimuth (see for instance the time span 21st to 24th of October 1995 in Figure 5). The dots corresponding to source area SEC2 cover a backazimuthal range from –45° to –75°. SEC2 also probably consists of two source subareas at about –50° and –66°. But the resolution is not sufficient to discriminate these subareas without doubt. Source area SEC3 covers the backazimuth range from –95° to –105° with a clearly preferred backazimuth of –100°. For the 22nd, 23rd and 26th, 27th of January 1996 an additional source at about –115° shows up in Figure 5. From the 3rd to the 5th of November two source areas at about –127° and –154° (SEC4 and SEC5) are clearly visible.

The constancy of the observed backazimuths means that the generation area of secondary microseisms is very probably not the storm centre itself. A clear observation in this respect could be made for the 16th and 17th of December 1995, a time span in which only the microseismic source SEC1 in northern direction (Figure 7b) was strongly active.

Figure 7a shows that the source area SEC1 started to dominate the microseismic wavefield on December 16th at about 6 UT (Universal time). The observed backazimuth then is constant (12° ± 5) until the morning of the next day. The centre of the cyclone moved in the same time span by more than 20° (shown in Figure 7b). In the second half of December 17th, while the cyclone itself had reached the continent, the scatter of the observed backazimuths is appreciably larger than the day before. At about 18 UT of December 17th a second source area started to show up under a backazimuth of about 20° to 25° corresponding to the direction of the Barents Sea/White Sea. The mean of the dots corresponding to the dominant source seems to move slightly from 12° to less than 10° in backaz-

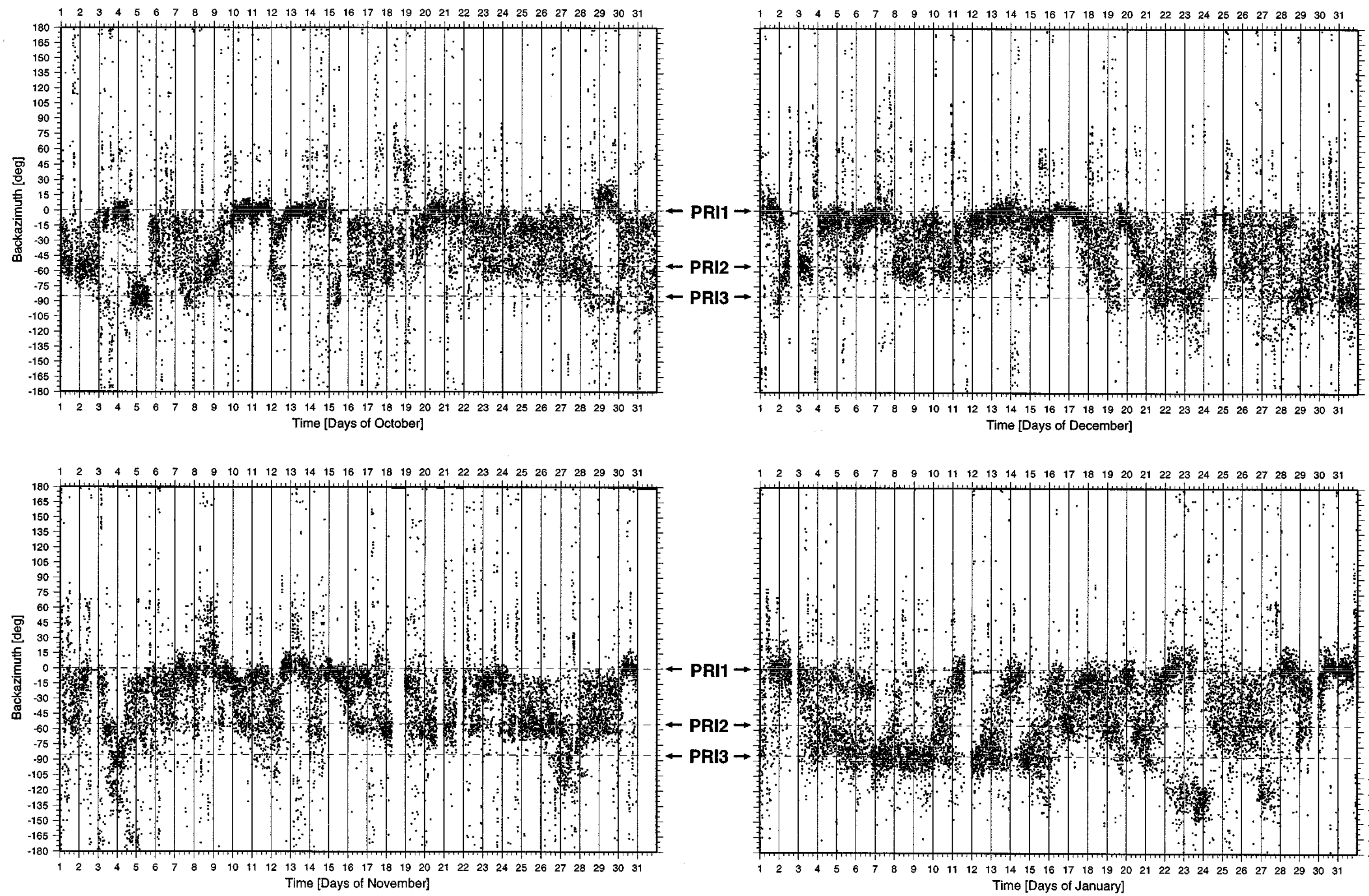

Figure 4. Backazimuths of primary microseisms reaching the GRF-array during October, November, December 1995 and January 1996.

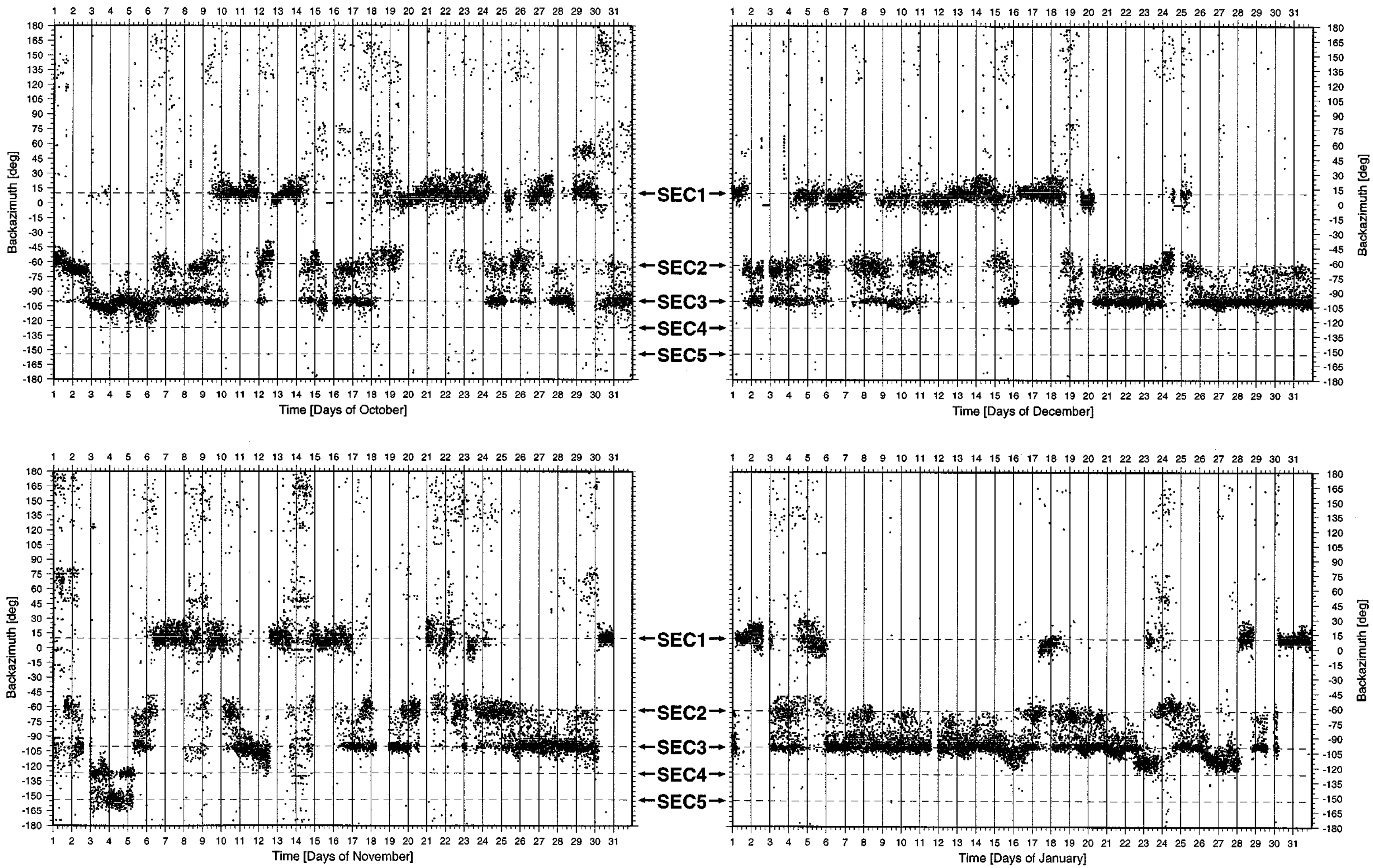

Figure 5. Same as Figure 4, but for secondary microseisms.

Table 1. Backazimuths of the detected primary and secondary microseismic generation areas

Microseisms	Area no.	Mean backazimuth	Backazimuth range	Direction from GRF
	PRI1	±0°	+10° . . . –25°	North-Norway
Primary	PRI2	–55°	–60° . . . –75°	British Isles
	PRI3	–85°	–75° . . . –100°	Wales/The Channel
	SEC1	+10°	+16° . . . –4°	North-Norway
	SEC2	–63°	–50° . . . –70°	British Isles
Secondary	SEC3	–100°	–95° . . . –105°	Bretagne
	SEC4	–127°	–122° . . . –132°	Biscaya/Algarve
	SEC5	–154°	–148° . . . –160°	West-Mediterranean coast

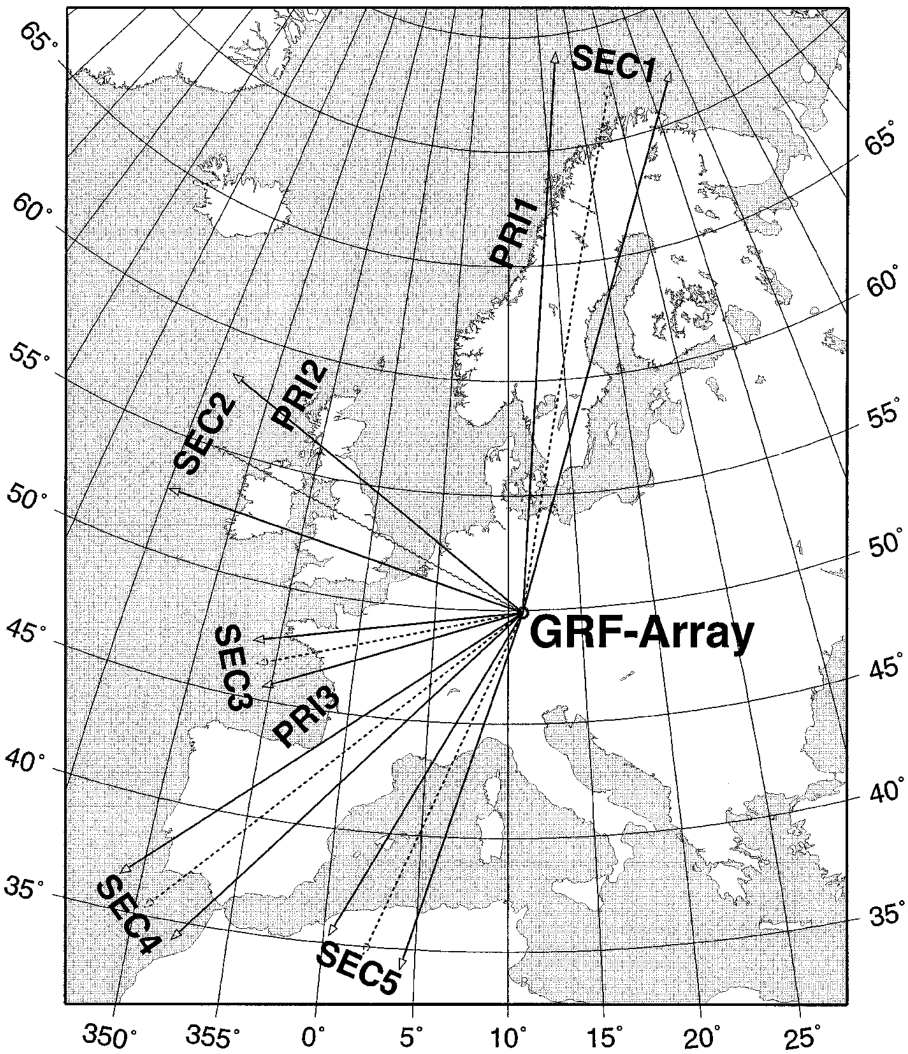

Figure 6. Backazimuths of the source areas of primary (PRI1–PRI3) and secondary (SEC1–SEC5) microseisms in a transverse mercator projection corresponding to Figures 4 and 5.

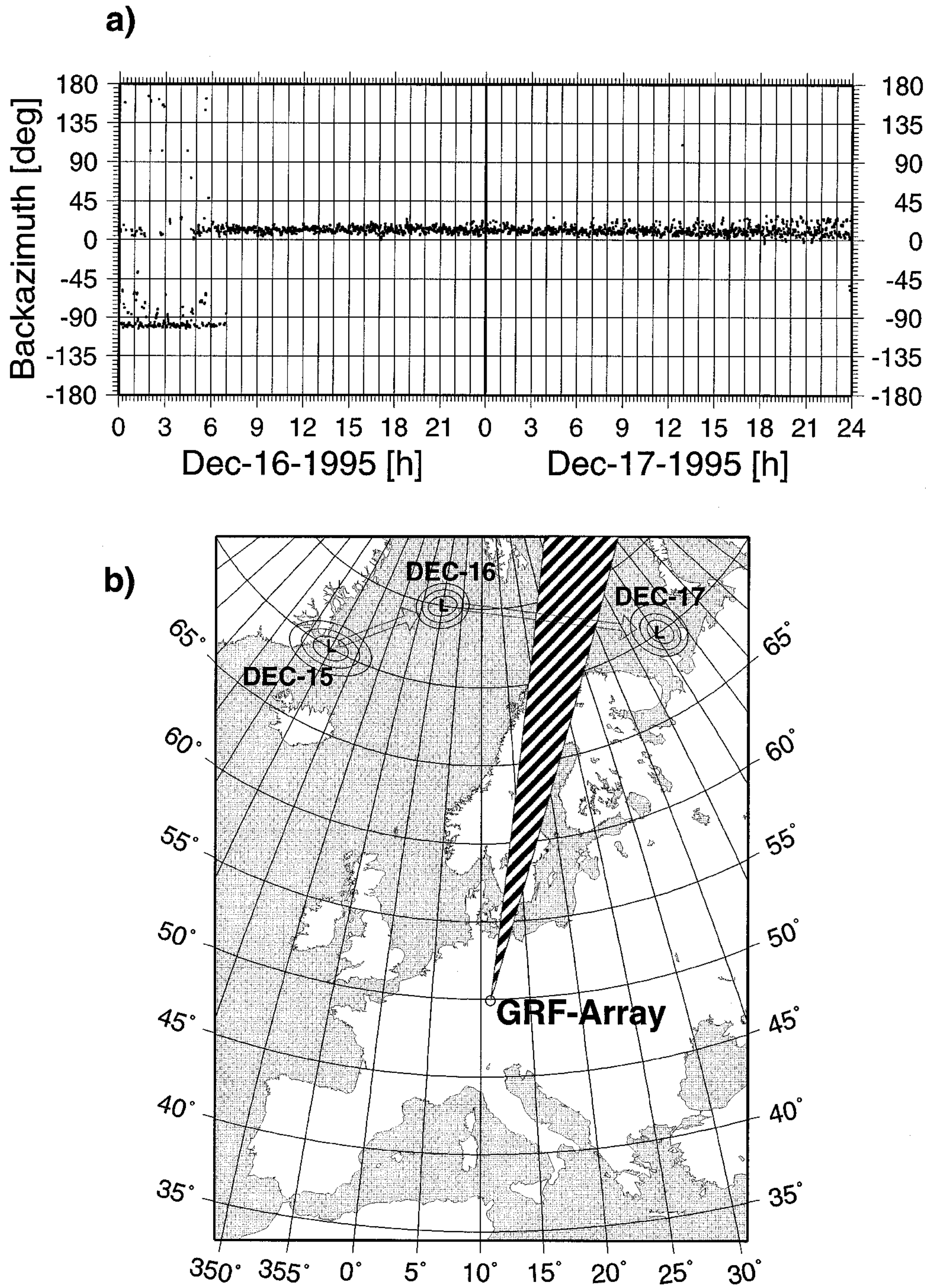

Figure 7. Backazimuths observed for the secondary microseismic wavefield during the 16th and 17th of December 1995. (a) Plot of the secondary microseisms backazimuths. (b) Course of the storm cyclone (L) in the same time span. The shaded area is the observed direction of the secondary microseisms.

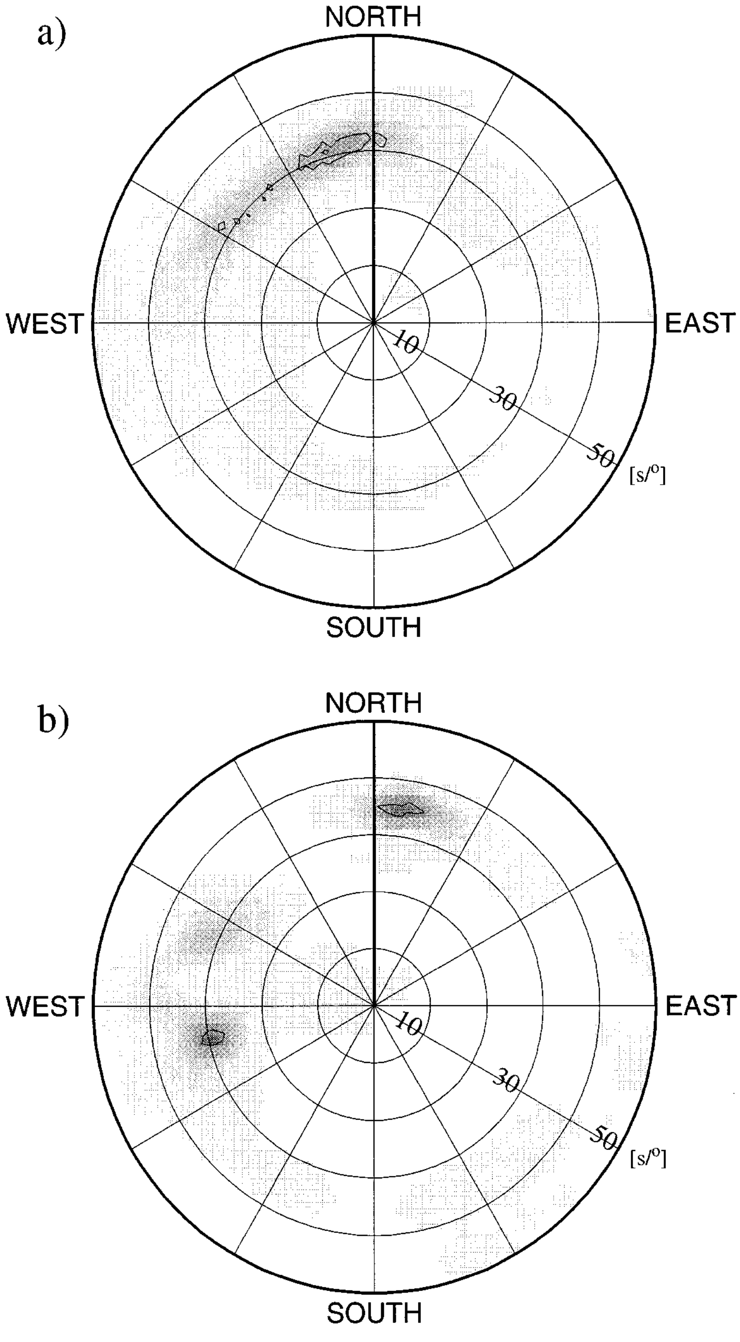

Figure 8. Cumulative plot of all frequency-wavenumber processing results for the timespan from October 1995 to January 1996 (backazimuth versus slowness). a) primary microseisms b) secondary microseisms The slowness grid in radial direction is in steps of 10 s/°. The contour line marks the level, where the density detections measured from the top of the respective peak in the slowness-backazimuth plane is 50% of the maximum level.

imuth at the end of December 17th but the scatter in the plots is too large to allow a decision.

Figure 8 shows the cumulative results of the frequency-wavenumber analysis for the timespan from October 1995 to January 1996 for primary (see Figure 8a) and secondary microseisms (see Figure 8b). From Figure 8b the two dominant source areas of secondary microseisms can be identified at backazimuths of about +10° and –100°. The other source areas are less pronounced in the cumulative plot due to their shorter durations of activity. The slowness for the secondary microseisms ranges from about 30 s/° to about 35 s/°. The primary microseisms in Figure 8a show the previously mentioned more broad azimuthal distribution ranging from about –70° to 10° im backazimuth. The corresponding slowness values concentrate near 30 s/°.

Distance estimation

Microseisms are mainly composed of surface waves. It is therefore not possible to derive the distance of the microseismic sources from the observed wave slowness values. To solve the location problem for sources of secondary microseisms, two different methods could be applied: 1) A triangulation using additionally the backazimuth determined by a second array and 2) a distance estimation using the dispersion of the water waves.

Distance estimation by triangulation

Additional to the GRF data broadband data of seven new installed broadband NORSAR stations (Fyen, 1994) were available and could be analyzed for the 31st January 1996, where the source SEC1 was also dominantly active (compare Figure 5). Using the observed backazimuths of 11° ± 3 at GRF and 20° ± 3 at NORSAR a triangulation could be performed. Despite of the disadvantageous geometry (see Figure 9) the source area could be constrained to lie near the north-Norwegian coast. The error-ellipse in Figure 9 represents the location error estimated from the errors in the backazimuth determination of both arrays.

Distance estimation utilizing the dispersion of ocean waves

The second method (according to Haubrich et al., 1963) utilises that for the generation of secondary microseisms similar periods of incoming and reflected waves are necessary. A characteristic feature of water (or gravity) waves is their dispersion, expressed in the equation:

$$\omega = \sqrt{g\,k\tanh(kH)} \tag{1}$$

(where ω is the angular frequency, g the gravity acceleration constant, k the wavenumber and H is the water depth).

In case of shallow water (typically $H < {}^1/_{15}$ of the wavelength λ), $kH \ll 1$ and thus $\tanh(kH)$ can be approximated by kH. Equation 1 then yields: (shallow-water-approximation)

$$c = \sqrt{gH}. \tag{2}$$

That means in shallow water waves show no dispersion and their phase velocity increases with water depth.

In deep water, i.e. when the ocean depth exceeds ${}^1/_3\lambda$, $kH \gg 1$ and thus $\tanh(kH) \approx 1$, the dispersion relation can be simplified to the well known deep-water-approximation:

$$c = \sqrt{g/k}. \tag{3}$$

When ocean waves reach beaches, they have travelled the path from their origin to the continent through deep water under dispersion (see Figure 12b for a scheme). Consequently first the low-frequency ocean waves reach the shores and progressively higher frequency waves arrive. Inserting Equation 3 into the equation for the group velocity of gravity waves ($c_g = {}^1/_2 c$) yields linearly increasing values for the frequency f with time t:

$$c_g = \frac{r}{t} = \frac{g}{4\cdot\pi\cdot f} \Rightarrow f = \frac{g}{4\cdot\pi}\cdot\frac{1}{r}\cdot t$$

$$\text{or } r_i = \frac{g}{4\cdot\pi}\cdot\frac{\Delta t_i}{\Delta f_i}, \tag{4}$$

where Δt_i and Δf_i are the observed travel times and dominant frequencies, respectively. Therefore the microseismic noise wavefield also shows a dispersive shift of its two centre peaks that rise progressively to shorter periods with time (see Figure 10). As the reflected water waves are again dispersed in deep-water, the necessary interference condition for the generation of secondary microseisms (oppositely travelling wave packets of similar periods) is given only in a sharply limited area (around point X in Figure 12b). At point X the incoming water waves have travelled the distance $(r - \Delta r)$ and have a peak frequency $(f + \Delta f)$ higher as the frequency f observed at the coast. The reflected waves have travelled a longer distance $(r + \Delta r)$ and due to dispersion the peak frequency is lowered to $(f - \Delta f)$. The group velocity of the incoming and reflected water waves is therefore:

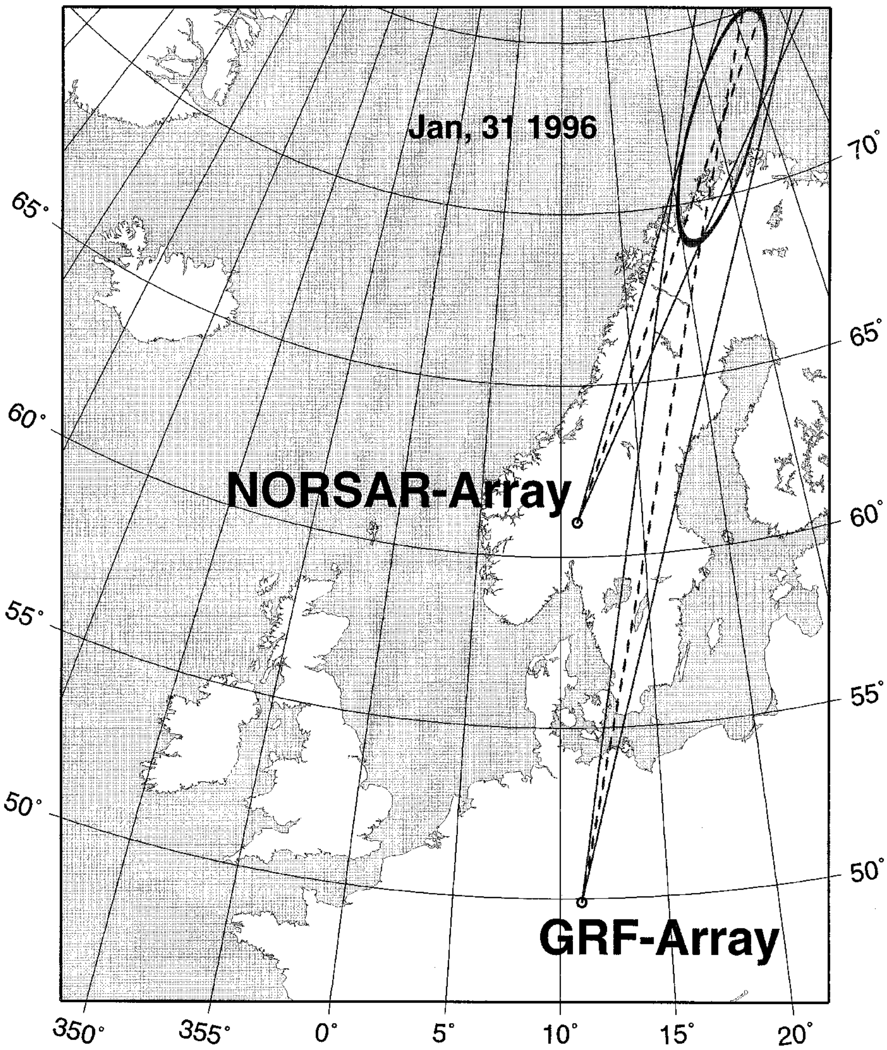

Figure 9. Location results of a triangulation using the seismic arrays NORSAR and GRF. The ellipse shows the location error estimation at the north Norwegian coast.

$$c_{\text{incoming}} = \frac{r - \Delta r}{t} = \frac{g}{4\pi(f + \Delta f)}$$

$$\Rightarrow (r - \Delta r) \cdot (f + \Delta f) = \frac{gt}{4\pi} \qquad (5)$$

$$c_{\text{reflected}} = \frac{r + \Delta r}{t} = \frac{g}{4\pi(f - \Delta f)}$$

$$\Rightarrow (r + \Delta r) \cdot (f - \Delta f) = \frac{gt}{4\pi}. \qquad (6)$$

Setting Equation 5 equal to Equation 6, multiplying and taking into account that Q is defined as $(f/2\Delta f)$ yields (for details see Haubrich et al., 1963):

$$\frac{2 \cdot \Delta f}{f} = Q^{-1} = 2 \cdot \frac{\Delta r}{r} \qquad (7)$$

where r is the distance between the origin of the wave packets (i.e. the storm cyclone) and the coast and Δr is the distance of the secondary microseisms generating area from the coast. The quality factor Q can be determined from the width of the primary spectral peak at f.

Figure 10 shows the centre peak periods observed for the 16th and 17th of December 1995. Three linear fits are plotted for corresponding primary and secondary periods to estimate the possible origin time range and thus the possible distance range r of the water wave

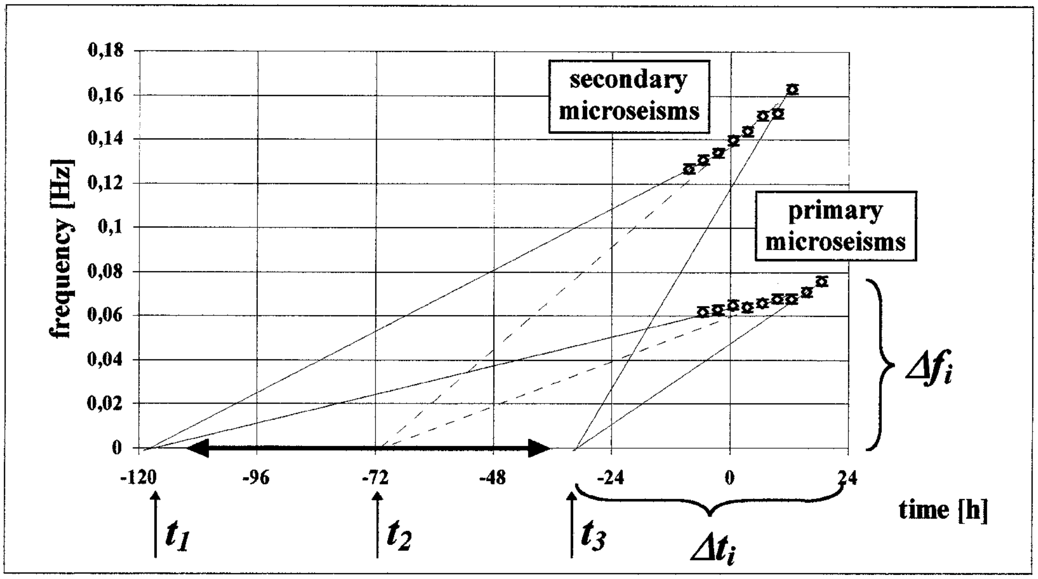

Figure 10. Dispersion data of water waves showing mean peak frequencies of primary and secondary microseisms versus time. A shift of the mean peak to higher frequencies with time is clearly visible. The time zero point is December 16th 1995, 0 UT. Three possible linear fits are suggested, yielding t_2 as a mean travel time of the dispersed water waves and t_1 as the maximum and t_3 as the minimum possible travel time. The inverse slope of a linear fit is thus $\Delta t_i / \Delta f_i$ and is used in Equation 4.

inducing cyclone. The inverse slopes of the linear fits $i = \{1, 2, 3\}$ in Figure 10 yield possible distances r of 1750 to 5000 km. Inserting the quality factor Q of 13.5 (computed from the width of the primary microseism spectral peak) for the 16th of December 1995 the source area could be determined to lie within a range of 65 to 185 km off the north-Norwegian coast.

A general estimation of the distance of the origin of secondary microseisms can be made, using the observation that the quality factor Q of the primary microseismic peak is always about 13 (Haubrich et al., 1963). An inspection of the weather maps throughout the observation period showed that the wave generating cyclones were not located more than 3500 km from the European coasts. Inserting this value into Equation 7 yields that secondary microseisms can be generated maximally 150 km offshore.

Characteristics of the generated waves

As mentioned above the two days of the 16th to 17th of December 1995 showed particularly coherent seismic waves (see Figure 3) coming from an extraordinarily powerful, separate source that is located in sector PRI 1/SEC1 in Figure 6.

At periods of primary microseisms the noise source had a mean backazimuth of 2°±7 from 10:00 UT on the December, 16th and during the whole next day. During this time the observed slowness values remained constant at 31.6 s/° ±1.1 on the Z-components for the GRF array data. Particle motion analysis on rotated traces in selected time windows showed a retrograde Rayleigh type motion. The slowness value observed with the ANISO network was slightly higher (32.9 s/° on the Z-components) indicating differences in the regional velocity structure.

The secondary microseisms arrived from a backazimuth of 12.0° ± 5.0 at GRF (compare Figure 7a, and 7.0° ± 5.0 at the ANISO network stations. A constant slowness of 35.5 s/° with a variance of ±0.7 s/° at GRF and 34.5 s/° ±1.0 at the ANISO network was measured on the Z-components during the same time span and the observed particle motion likewise was retrograde. The slowness values and the particle motion indicate that the primary and secondary coherent noise wave field consists of fundamental mode Rayleigh type surface waves. F–k analysis of seismograms on the E-components of the ANISO network stations (almost naturally rotated for transversal waves arriving from the sources PRI1/SEC1 and therefore corresponding to SH-type motion) showed a dominant slowness of

29.0 s/° for primary microseisms and 30.0 s/° for secondary microseisms. These slowness values are consistently slightly smaller compared to the results for the Z-components and thus a strong indication for the observation of Love waves because the group velocity of Love waves is higher for continental paths in the period ranges of interest.

Both the backazimuth error and the slowness error are about equal to the resolution limits given by the grid distance in slowness space for a source in northern direction (see also Section 2). That means that for this particular time span we can use the backazimuth error to limit the maximal spatial extension of the source in east-west direction to be less than about 200 km.

Relative energy ratios

The nature of a seismic source can very often be characterized by the relative amount of generation of waves of P/SV and SH type. It is therefore essential to determine in what ratio coherent Rayleigh and Love waves are generated by the source.

The sum over the squared amplitudes of the velocity proportional seismogram samples is proportional to the energy in the corresponding seismic wave. The amount of the coherent energy E can be estimated from the array beam in the time domain:

$$E = c \cdot \frac{1}{N} \sum_{i=1}^{N} a_i^2, \tag{8}$$

where c is an arbitrary proportionality constant, i is the running index of samples in the beamtrace, a is the amplitude of sample i and N is the number of samples in each seismogram. While the coherent energy is determined by Equation 8, the relative magnitude of the total energy can be approximated by $c \cdot \frac{1}{M} \sum_{j=1}^{M} \frac{1}{N} \sum_{i=1}^{N} a_{ij}^2$, where M is the number of seismogram traces. For the primary microseismic wavefield the relative amount of coherent energy reaches up to 82% for the GRF-array data and up to 61% for the ANISO network data. The coherent energy is relatively smaller for the secondary microseisms (GRF: 64%, ANISO: 36%), which can partly be explained by the larger scatter of the shorter period secondary microseisms due to crustal heterogeneities. The observed Love waves (on the E-components) show consistently smaller relative amounts of coherent energy (41% for primary and 16% for secondary microseisms). Table 2 shows the amount of coherent energy of source SEC1 on December 16th, 1995 from 19:00 UT to 20:00 UT relative to the total energy of the microseismic wavefield.

Table 2. The relative amount of coherent energy of the primary and secondary microseismic wavefield on December 16th 1995

Microseisms	Array	Z-component	E-component
Primary	GRF	82%	–
	ANISO	61%	41%
Secondary	GRF	64%	–
	ANISO	36%	16%

Taking the ratio of the coherent energy values E (Equation 8) of the naturally rotated transversal beam trace to the vertical beam trace, the proportionality constant c in Equation 8 cancels out yielding the energy ratio of coherent Love and Rayleigh waves. For the estimation of this energy ratio 10 out of 25 broadband stations of the ANISO network were used (see Figure 2). The energy ratio of transversal to vertical energy yielded 1.2 for the primary noise wavefield and 0.25 for the secondary noise wavefield. That means that there is a much higher relative content of coherent Love wave energy in the primary microseisms than in the secondary microseismic noise wavefield, indicating the different source mechanisms.

Discussion

Water waves

Gravity waves propagate in deep water as Rayleigh waves and therefore the orbits of water particles describe circles (Figure 11a). In a water column all water particles are in phase, thus they cause pressure perturbations. Because their orbit radiuses decrease exponentially with depth, the pressure perturbation also decays proportional to $\exp(-kH)$. Thus in deep water only a negligible part of the direct pressure perturbation reaches the ocean bottom. For example, in a depth of half the wavelength the pressure change reaches only 4% of its surface magnitude and in a depth of twice the wavelength no pressure change can be measured at all. For predominant ocean waves, half of the wavelength is about 150 m, which is roughly the depth of the European continental shelf. That means, above shelf areas ocean waves act as deep water waves and do not feel the effects of the ocean bottom.

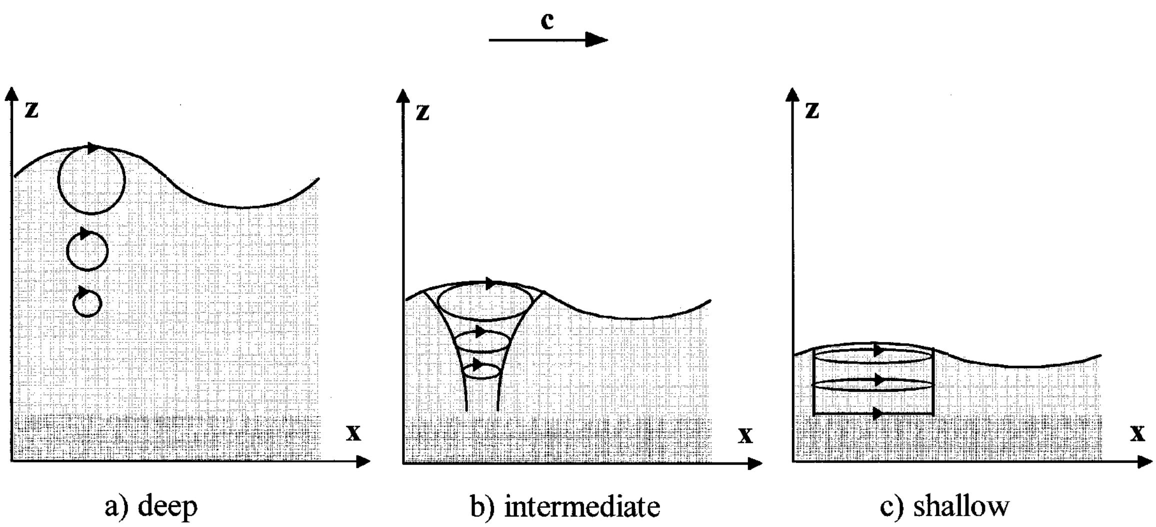

Figure 11. Trajectories of water particles in (a) deep, (b) intermediate and (c) shallow water. In shallow water vertical and horizontal ground motions are generated.

Primary microseisms

However, if the waves arrive at the beaches, where the shallow-water-approximation is applicable, the pressure changes propagate unattenuated to the ocean bottom and a powerful excitation of vertical primary microseisms takes place (see Figure 12a). The preferred areas of primary microseisms shown in Table 1 should therefore be regions where high water wave amplitudes can be observed at beaches or steep coasts.

Moving into regions of shallow water the circular trajectories mutate more and more to ellipses (Figures 11b and 11c). Because of friction of water particles at the ocean bottom, horizontal ground motion is generated immediately at coasts. While the vertical pressure can be modelled by a time varying vertical single force, the friction causes a horizontal movement of the ground which can be modelled by a horizontal single force. The vertical force is only capable to generate Rayleigh waves, but the horizontal force also radiates Love waves. The relative amplitude ratio of Love and Rayleigh waves corresponds to the height of the waves, the water depth in the shallow water region, the friction at the ocean bottom and the source-receiver geometry. The horizontal force is always directed perpendicular to the coastline. Considering the special geometry for the source acting at the Norwegian coast the radiation pattern of a horizontal single force component would be favourable for the generation of Love waves in the direction of the GRF-array.

Secondary Microseisms

In the following equation derived by Longuet-Higgins $\overline{p_H}$ denotes the mean pressure acting on the ocean bottom at depth H. A_1 and A_2 are the amplitudes at the free water surface in the wavetrains with opposite travelling directions, ρ is the density of water, p_η is the ambient pressure on the surface at height η and t denotes time.

$$\frac{\overline{p_H} - p_\eta}{\rho} - gH = -2A_1A_2\omega^2\cos(2\omega t). \qquad (9)$$

In the case that one of the amplitudes of the interfering wavetrains is equal to zero (comparable to a single progressive wave) the complete right-hand side of Equation 9 vanishes. Then the mean pressure p_H on the bottom is constant and no secondary microseisms are produced. If both amplitudes are equal $A_1 = A_2 = A$, the mean pressure at the ocean bottom varies with an amplitude proportional to the square of the wave amplitude and with twice the frequency (or half the period) of the original water wave.

The higher coherency observed and the small scatter of the energy maxima with respect to the backazimuth both are indications for a small lateral extension of the source area. Due to the quadratic form of the excitation term the regions with the highest standing wave amplitudes will dominate the microseismic wavefield. This is an explanation for the observation that the secondary microseisms arrive from discrete backazimuths, while the distribution of primary microseisms

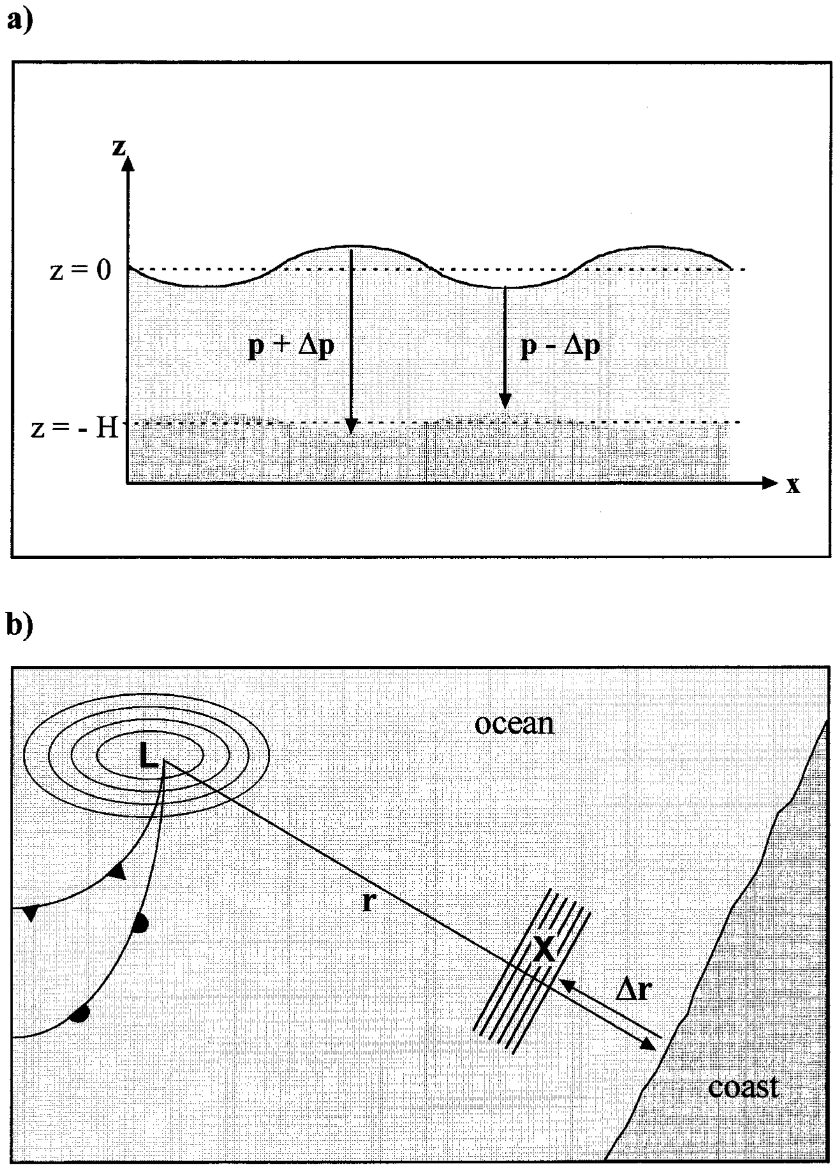

Figure 12. Schemes for the generation of primary and secondary microseisms. a) Primary microseisms can only be generated in coastal regions in shallow water. Here water wave energy can be converted directly into seismic energy through vertical pressure variations that have the same period as the water waves. b) Secondary microseisms are generated, when ocean waves with the same period, but opposite directions interact at point X. The interfering waves produce a standing wave with half the period of the ocean waves. The cyclone is marked with L. The distance to the coast is denoted with r and Δr is the distance to the point of interference (X).

(depending only linearly on ocean wave amplitude in shallow-water-approximation) is more continuous.

The small but not negligible amount of secondary Love waves observed for the source SEC1 could be caused by scattering of Rayleigh waves in the source region. More 3-component array data are needed to distinguish between scattering in the source area and a possible contribution of a yet unknown source term.

The location of the generating area for secondary microseisms using the triangulation method yielded that the source SEC1 was located northwest of the northernmost tip of Norway near Hammerfest. The centre of the location error ellipse (see Figure 9) lies

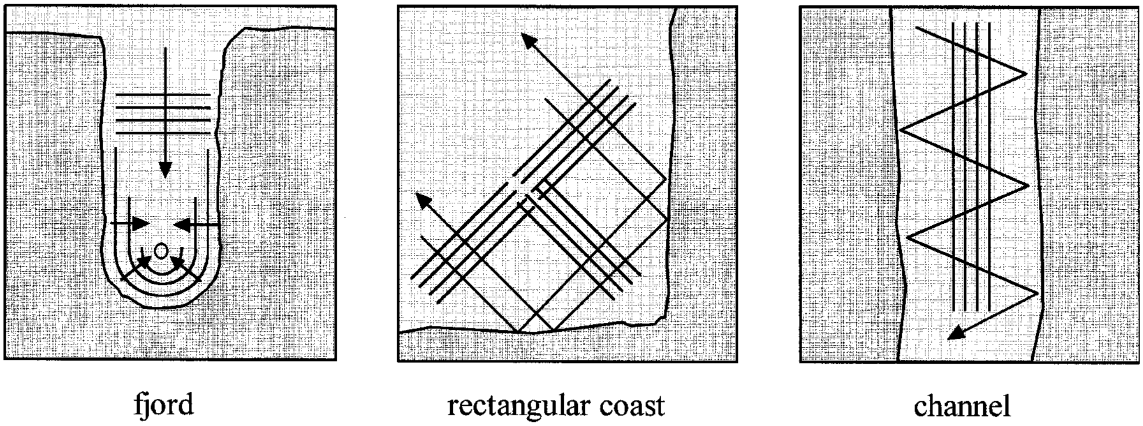

Figure 13. Figure 13: Examples for coastline geometries that provide the necessary interference condition for the generation of secondary microseisms.

about 100 km away from the coast. This is in good agreement with the distance from the coast calculated using the water wave dispersion method. A possible generation area is therefore the shelf region north of the coast. However, the error ellipse covers also the north-Norwegian coast. The landscape of the shore in northern Norway is characterized by steep coasts and elongated fjords with a length of tenth of kilometres and a water depth of more than 200 m. The openings of these fjords point toward northern directions. Therefore we think that it is at least likewise plausible that the ocean waves moving into these fjords from northerly directions can produce standing waves of considerable amplitude in certain fjord sections. Resonance phenomena in water filled channels are a well known fact (see Landau-Lifschitz, 1951; Benjamin & Ursell, 1954; Ben-Menahem & Singh, 1981). Figure 13 shows possible coastline geometries providing the necessary constraints for the generation of standing waves.

The location result using the dispersion of water waves does not contradict this hypothesis, because only the relative distance between the reflection point and the generating area is determined with this method. If the reflection point is situated more inland in the fjord systems, the found distance limit (150 km) not necessarily needs to be offshore but also could be located behind the coastline.

More observations using medium aperture 3-component broadband arrays are necessary to obtain more precise source locations and extension limits of the source areas which radiate strong coherent waves. Such experiments should also allow to constrain the force model of the microseismic sources better.

Conclusions

Broadband data of the medium aperture GRF array in Germany were analyzed with $f-k$ analysis for a time span of four months in winter 1995/96.

Five discrete generating areas for secondary microseisms and three generating areas for primary microseisms were found. While backazimuths observed for the primary microseisms show a wide scatter, the backazimuths for the secondary microseisms are much more concentrated. In no case we could observe a continuous movement of the microseismic sources with the generating storm cyclone.

The location of the strongest source for secondary microseisms using an approach utilizing the dispersion of the water waves (Haubrich et al., 1963) leads to a source distance within 150 km north of the north-Norwegian coast. This location could be confirmed by a triangulation using additionally the NORSAR array, but the location-error ellipse also covers inland area behind the Norwegian coast.

Investigation of the ratios of coherent energy on the vertical and horizontal traces yields a much higher relative amount of Love waves with respect to Rayleigh waves for the primary microseismic wavefield. This difference is probably caused by the presence of a horizontal force component in the swell of ocean waves on beaches or steep coasts.

We propose that the dominant part of the secondary microseismic wavefield is not generated by deterministic or statistical fluctuation of the ocean waves in the storm centre itself, but that the interaction of the incoming ocean waves and local geometrical structures cause standing wave patterns of considerable height in cannels or fjords (compare Figure 13) generating in turn the most powerful secondary microseisms.

More observations with medium aperture broadband arrays with better azimuthal coverage are necessary to obtain more precise locations for the source areas.

Acknowledgements

This work is based on a diploma thesis at the Physics department of the Friedrich-Alexander-University Erlangen-Nürnberg. We like to express our thanks to the staff of the Gräfenberg-array financed by the Bundesanstalt für Geowissenschaften und Rohstoffe and the Deutsche Forschungsgemeinschaft, J. Klussmann for sending literature and weather maps and J. Fyen for providing the NORSAR data. This work would not have been possible without technical support from the SZGRF Erlangen.

References

Båth, M. & O. Kulhánek, 1990. Long-period microseisms at UmeÂ, Sweden. Phys. Earth Planet. Int. 63: 232–233.

Benjamin, T. B. & F. Ursell, 1954. The stability of the plane free surface of a liquid in vertical periodic motion. Proc. r. Soc. Lond. A 255: 505–515.

Ben-Menahem, A. & Sarva Jit Singh, 1981. Seismic waves and sources, Chapter 9.3: Gravity waves in liquids. Springer-Verlag, New York: 776–796.

Bungum, H., E. Rygg & L. Bruland, 1971. Short period seismic noise structure at the Norwegian seismic array. Bull. Seism. Soc. Am. 61, No. 2: 357–373.

Bungum, H., S. Mykkeltveit & T. Kværna, 1985. Seismic Noise in Fennoscandia, with emphasis on high frequencies. Bull. Seism. Soc. Am. 75, No. 6: 1489–1513.

Capon, J., 1972. Long-period signal processing Results for LASA, NORSAR and ALPA. Geophysic Journal Roy. astronomical Soc. 31: 279–296.

Cessaro, R. K. & W. W. Chan, 1989. Wide-angle-triangulation array study of simultaneous primary microseism sources. J. geophys. Res. 94, No. B11: 15555–15563.

Darbyshire, J., 1950. Identification of microseismic activity with sea waves. Proc. r. Soc. Lond. A 202: 439–448.

Darbyshire, J., 1991. A further investigation of microseisms recorded in North Wales. Phys. Earth Planet. Int. 67: 330–347.

Fyen, J., 1994. Improvements and Modifications. NORSAR Scientific Report No. 2–93/94, Kjeller, Norway: 62–73.

Gutenberg, B., 1924. Die seismische Bodenunruhe. Sammlung Geophysikalischer Schriften Nr. 3: 1–69. (In German)

Harjes, H. P. & D. Seidl, 1978. Digital recording and analysis of broadband seismic data at the Gräfenberg (GRF) array. J. geophys. Res. 44: 511–523.

Hasselmann, K., 1963. Statistical analysis of the generation of microseisms. Rev. Geophys. 1: 177–210.

Haubrich, R. A., W. H. Munk & F. E. Snodgrass, 1963. Comparative spectra of microseisms and swell. Bull. Seism. Soc. Am. 53: 27–37.

Holcomb, L. G., 1989. Seismic Noise. Encyclopedia of solid Earth Geophysics: 1089–1092.

Iyer, H. M., 1958. A study of direction of arrival of microseisms at Kew Observatory. Geophys. J. 1: 32–43.

Kværna, T. & F. Ringdahl, 1986. Stability of various $f - k$ estimation techniques. NORSAR Scientific Report No. 1–86/87: 29–40, Kjeller, Norway.

LaCoss, R. T., E. J. Kelly & M. N. Toksöz, 1969. Estimation of seismic noise using Arrays. Geophysics 34, No.1: 21–38.

Landau-Lifschitz, 1951. Vol. VI, Hydrodynamik. Akademie Verlag GmbH, Berlin: 47–48, (In German).

Longuet-Higgins, M. S., 1950. A Theory on the origin of microseisms. Philos. Trans. R. Soc. Lond. A. 243: 1–35.

Schmalfeldt, B., 1978. Ein Vergleich von Mikroseismik und Seegangsspektren und ein Versuch die Anfachungsgebiete zu lokalisieren. Hamburger Geophysikalische Einzelschriften, Heft 35, (in German).

Strobach, K., 1962. Ein Beitrag zum Problem der Entstehung und der Wellennatur der mikroseismischen Bodenunruhe. Hamburger Geophysikalische Einzelschriften, Heft 5, (in German).

Wiechert, E., 1904. Verhandlungen der zweiten internationalen Seismologischen Konferenz. Gerlands Beitr. Geophys., Ergänzungsband. II: 41–43 (in German).

Wielandt, E. & J. M. Steim, 1986. A digital very-broad-band seismograph. Ann. Geophys. 4B: 227–232.

Wielandt, E. & G. Streckeisen, 1982. The leaf spring seismometer: Design and Performance. Bull. Seism. Soc. Am. 72, 6: 2349–2367.